Received: 13 March 2024 | Revised: 17 June 2024 | Accepted: 3 July 2024
DOI: 10.1002/aoc.7639

FULL PAPER

Applied Organometallic Chemistry WILEY

MnO$_2$@Al-BDC nanocomposite as adsorbent of remarkable high efficiency toward iron remediation from wastewaters

Mohamed I. Said[1] | **Marwa Sayed**[2] | **Aref A. M. Aly**[1] | **Muhammad Atef**[3]

[1]Chemistry Department, Faculty of Science, Assiut University, Assiut, Egypt
[2]Drinking water and sewage company in Assiut, Egypt
[3]Environmental Affairs at Assiut & New Valley Company for Water&Wastewater, Egypt

Correspondence
Mohamed I. Said, Chemistry Department, Faculty of Science, Assiut University 71516, Assiut, Egypt.
Email: mmegeed2017@gmail.com; mohamedali123@aun.edu.eg

Global environmental problems, especially those related to water contamination brought on by rapid industrialization and economic growth, are among the most dangerous threats facing humanity today. In this research work, Al^{3+} based metal–organic framework with 1,4-benzenedicarboxylic acid (H$_2$BDC) linker has been synthesized by a simple and economic coprecipitation method. The obtained Al-BDC MOF was utilized as an adsorbent for sequestering iron from wastewater, but only 54.0% of iron concentration was eliminated after 120 min. To boost the removal efficiency, modification of the Al-BDC MOF was carried out. MnO$_2$@Al-BDC nanocomposite was prepared and applied as a nanoadsorbent for iron remediation from water. The adsorption capability of Al-BDC MOF was greatly enhanced by facile modification. The adsorption efficiency reached 97.0% using 35.0 mg of the nanocomposite after 120 min compared to 54.0% iron removal using the un-modified MOF. The effect of pH of the medium was then studied using MnO$_2$@Al-BDC nanocomposite. The best elimination efficacy of iron was accomplished at pH $\sim$ 2.2. The adsorption of iron on the surface of MnO$_2$@Al-BDC nanocomposite attains 97.0% (120 min) using a 35.0 mg dose of adsorbent and reaches 98.7% utilizing a 50.0 mg dose of adsorbent. In contrast, at pH $=$ 9.2, the removal efficiency drops to 90.0% (after 120 min, 35.0 mg adsorbent). The adsorption capability was examined also using a variety of iron concentrations, i.e., 2.5, 5.0, and 7.5 mg/L where the adsorption efficiency dropped notably upon increasing the concentration. It dropped from 96.3% to 87.0% using 35.0 mg of MnO$_2$@Al-BDC nanocomposite at 90 min. The newly developed adsorbent showed a pronounced efficiency for Fe^{3+} removal against real samples collected from different water sources. Ultimately, this research introduces a novel MnO$_2$@Al-BDC nanocomposite, synthesized through a simple and economical coprecipitation method, to address water contamination by iron. The innovation lies in the significant enhancement of iron elimination efficiency, from 54.0% with unmodified Al-BDC MOF to 97.0% with the MnO$_2$@Al-BDC nanocomposite.

KEYWORDS

Al-BDC MOF; Fe^{3+} elimination, heavy metals adsorption; MnO$_2$ nanocomposites; water pollution

https://doi.org/10.1002/aoc.7639

1 | INTRODUCTION

Metal–organic frameworks (MOFs) are a type of porous material that have garnered significant interest in recent years. They are constructed from metal ions or clusters coordinated with organic ligands producing a crystalline three-dimensional network structure. MOFs exhibit exceptional structural diversity, with a broad range of compositions, pore sizes, and surface areas.[1] The unique properties of MOFs arise from their modular and tunable nature. The choice of metal ions and organic ligands allows for precise control over their structure, porosity, and functionality. MOFs can be designed to have high surface areas, large pore volumes, and specific chemical properties, making them versatile materials with numerous applications.[2] Moreover, MOFs find many applications in gas storage,[3] drug delivery,[4,5] sensing and fluorescence,[6,7] catalysis,[8] chemical separation, water harvesting, and more. Their diverse functionalities make them attractive for a wide range of industries, including energy, pharmaceuticals, environmental monitoring, and chemical manufacturing.[9]

MOFs have proven to be quite promising for water remediation due to their unique properties and large surface area. MOFs can selectively adsorb and remove various contaminants from water, including heavy metals,[10–12] organic pollutants,[13] dyes,[14] pharmaceuticals,[15,16] and even radioactive species.[17] The large surface area and tunable pore structures of MOFs enable high adsorption capacities and efficient removal of target contaminants.[18] MOFs can effectively capture heavy metal ions, such as lead, cadmium, mercury, and arsenic, from water.[19] MOFs are able to form strong coordination bonds with metal ions, facilitating their removal from aqueous solutions. MOFs with tailored pore sizes and functional groups can enhance the selectivity and efficiency of heavy metal ions removal. Typical examples of MOFs applications are frequently encountered in literature. An adsorbent (magnetic *Luffa*@MOF-199) was synthesized and used for separation–preconcentration of Ni (II), Pb (II), Cr (III), and Cd (II) in food, tobacco, and wastewater samples as 2-nitroso-2-naphthol chelates.[20] A review was published that describes recent developments in the use of MOFs in the analysis of toxic metals in food and environmental samples.[21] In other work dried water hyacinth was utilized as a biosorbent for removal of Cd (II) and Pb (II).[22] Furthermore a new adsorbent denoted as PCN-222-MBA (thiol-functionalized PCN-222) was designed and constructed by functionalizing Zr_6-nodes of PCN-222 (PCN = porous coordination network) with 4-mercaptobenzoic acid (MBA) that attained both selective and facile extraction of gold ions from aqueous medium.[23] In this context, a porous MOF was developed that comprises pyridyltriazol functionalized zirconium metal–organic framework which proved to possess remarkable efficiency for solid phase extraction of palladium ions from aqueous media.[24] A composite, $GO/Fe_3O_4/OPO_3H_2$/PCN-222, was synthesized via graphene oxide (GO) modification with magnetic particles, phosphorous-containing groups, and a mesoporous Zr-MOF, PCN-222. This solid was then used for dispersive solid phase extraction of uranium ions dissolved in water.[25]

Pollution of water and wastewater with heavy metal ions is a global issue brought on by the rapid growth of industrialization.[26] These metal ions besides being highly toxic to aquatic and territorial life, pose a serious risk to human health and the environment. Water supply pipes, mining, alloy production, plating plates, and metal finishing all deliver heavy metal ions into the environment.[27] Because they do not undergo biodegradation, heavy metals can readily infiltrate the food chain and accumulate in living things, where they can have increasingly harmful effects. The central nervous system, digestive tract, brain, cardiovascular, and endocrine systems can all be harmed by heavy metal ions. Anemia, sleeplessness, agitation, hallucinations, kidney damage, nausea, asthma, lung irritations, paralysis, diarrhea, low blood pressure, weight loss, heart failure, bronchitis, bone abnormalities, gene mutation, and cancer are among the hazardous effects of these ions.[26,27]

In biological and environmental systems, iron is one of the most vital elements that of utmost importance for humans and other living things.[28] Selective detection of iron is essential for living things since a lack or excess of Fe^{3+} ions can result in several physiological issues.[29] One of the promising recommended methods for removing heavy metal ions from water is the adsorption of these hazardous elements utilizing MOF-based adsorption technology, nevertheless, there is a need to increase their adsorption capacity.[30] Accordingly, in this work we explore the efficiency of a composite that originates from the MOF in the removal of iron ions from wastewater.

There are two methods to perform a modification to MOFs, i.e., in situ and ex-situ. In situ-MOF refers to the synthesis or formation of metal–organic frameworks (MOFs) directly within a specific environment or under specific conditions. Exo-MOF points to a type of metal–organic framework (MOF) structure that exhibits an exohedral or external surface functionalization. In the case of exo-MOFs, the external surface of the MOF structure is modified or functionalized with various groups or molecules.[31] This surface modification can be accomplished via post-synthetic methods, wherever the MOF is synthesized first and then subjected to a surface modification step. Alternatively, it can be attained via in situ synthesis, where the functional groups are incorporated during the MOF formation process.

The exo-functionalization of MOFs offers several advantages. It can significantly boost the stability of the MOF structure, improve its selectivity toward specific molecules, and enable the attachment of additional functionalities or molecules to achieve specific applications. For example, the introduction of functional groups on the external MOFs surface facilitates the adsorption or separation of target molecules, enhances catalytic activity, or enables the attachment of biomolecules for biomedical applications. Overall, exo-MOFs provide a versatile platform for tailoring the properties and functionalities of MOFs, expanding their applicability in areas such as sensing, catalysis, and drug delivery.

In this work, a porous aluminum metal–organic framework (Al-BDC) based on Al (III) and 1,4-H_2BDC was synthesized. Its modification was achieved via surface functionalization with MnO_2 by a very simple and economic method, and then applied as an adsorbent for iron removal from water. The results revealed that MnO_2@Al-BDC nanocomposite has better adsorption characteristics and attributes than Al-BDC MOF. Moreover, MnO_2@Al-BDC nanocomposite is very economic and can easily be prepared and the iron removal effectiveness remarkably increases at room temperature as the incremental dose of the composite increases without the need for heating or changing the pH. It is effective for all scales of iron concentrations as well and this particular type of adsorbent exhibits exceptional efficacy in eliminating Fe (III) from water, which has a broad potential of applications and a value for further studies. Furthermore, the adsorption mechanism and kinetics were investigated.

2 | EXPERIMENTAL

2.1 | Materials

The study's analytical-grade compounds were employed without any additional purification. The following chemicals were obtained from Sigma-Aldrich Chemie GmbH, Germany: aluminum chloride hexahydrate ($AlCl_3.6H_2O$), sodium hydroxide (NaOH, ≥ 97.0%), 1,4-Benzendicarboxylic acid (H_2BDC, ≥ 98.0%), ferric chloride ($FeCl_3$, ≥ 98.0%), potassium permanganate ($KMnO_4$, ≥ 97.0%), manganese chloride tetrahydrate ($MnCl_2.4H_2O$, ≥ 98.0%), hydrochloric acid (HCl, 37.0%), hydroxylamine (NH_2OH, 98.0%), and phenanthroline.

2.2 | Synthesis of Al-BDC MOF

Al-BDC MOF was prepared by mixing (1.0 g) 1,4- benzenedicarboxylic and (0.5 g) NaOH in 70.0 mL distilled water, with continuous stirring. Then (1.5 g) $AlCl_3.6H_2O$ dissolved in 30.0 mL distilled water was added, keeping the stirring of the reaction mixture for 2 h at ambient temperature. The obtained precipitate was isolated by centrifugation, washed many times with distilled water, and dried in air then in an oven at 60 °C.

2.3 | Synthesis of MnO_2@Al-BDC

MnO_2@Al-BDC nanocomposite was obtained by the simple exo-situ method. In a 250.0 mL beaker, 0.4 g of Al-BDC MOF in 100.0 mL distilled water was stirred for 10 min. Thereafter 0.4 g of $MnCl_2.4H_2O$ was added and the mixture was stirred for 30 min prior to the introduction of 0.06 g of $KMnO_4$. Subsequently, the mixture was strongly stirred for 1.0 h at ambient temperature. The obtained MnO_2@Al-BDC nanocomposite was centrifuged, washed frequently with water, and left to dry in air and then finally in an oven at 60 °C.

2.4 | Iron removal experiments

A stock of solution of 100.0 mg/L of $FeCl_3$ was first prepared. To a 50.0 mL of an aqueous solution of Fe^{3+} (5.0 mg/L), 35.0 mg of MnO_2@Al-BDC nanocomposite was introduced and stirred at ambient temperature. At proper intervals of time, the nanocomposite particles were filtered off. The clear solution was analyzed after that for the remaining iron concentration following the standard phenanthroline method (3,500-Fe B),[32,33] and using UV–vis spectrophotometry at λ_{max} of 510 nm. The whole experimental procedure was repeated at various time intervals. The initial Fe^{3+} concentration was determined per the same method.

In this method, Fe^{3+} was reduced to Fe^{2+} by boiling with HCl and hydroxylamine. It was then reacted with 1,10-phenanthroline (pH 3.2 to 3.3) where a red-orange complex was formed. For this colored solution, Beer's law is applied; its intensity does not depend upon the pH change from 3.0 to 9.0. A pH of 2.9–3.5 guarantees quick color formation when there is an excess of phenanthroline present. For at least six months, color standards remain consistent.

The influence of pH, adsorbent weight, initial Fe^{3+} concentration, and temperature were examined.

2.5 | Application to real water samples

Sample collection and preparation: Real water samples were collected from various sources from Assiut governorate-Egypt, including drinking and groundwater sources, with known contamination of Fe^{3+} ions. The samples were filtered to remove suspended particles before analysis.

2.6 | Physical measurements

Refer to the supporting information for the specifications of the instruments used to characterize and analyze the material.

3 | RESULTS AND DISCUSSION

3.1 | Characterization of the Al-BDC and MnO_2@Al-BDC

The reaction between aluminum ions and H_2BDC produces Al-BDC MOF with a formula of $[Al (BDC)OH]_n$, the composition of the MOF was investigated via elemental analysis where the data obtained display a congruence between the calculated and found elemental percentages of carbon and hydrogen. **C: calcd; 46.12 (found 46.11) and H: calcd; 2.40 (found 1.70)**.

IR analysis was then performed on the synthesized Al-BDC MOF and its nanocomposite with MnO_2 and the obtained spectra are shown in Figure 1. Two absorption bands can be seen at 1610 and 1415 cm^{-1} in the IR spectra of Al-BDC MOF and MnO_2@Al-BDC nanocomposite that are ascribed to the OCO asymmetric and symmetric stretching vibrations in the carboxylate group, respectively. These peaks corroborate the coordination of COO^- groups to the central aluminum.[34] The small absorption peak found at 1582 cm^{-1} is correlated with the C=C vibration in the linker. The absorption bands at 1698 and 3427 cm^{-1} are affiliated to the bending and stretching modes of water, respectively.

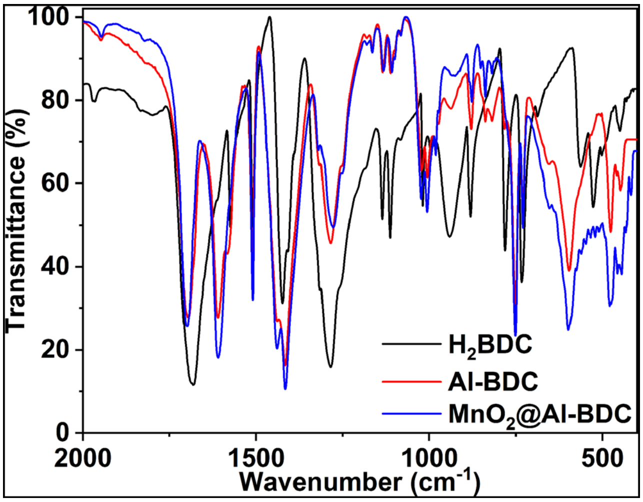

FIGURE 1 IR spectra of 1,4-H_2BDC, its Al-MOF and MnO_2@Al-MOF nanocomposite.

Furthermore, the band located at 1006 cm^{-1} is associated with the bending vibration of the $AlO_4(OH)_2$ μ_2-hydroxo groups, whereas the band found at 3680 cm^{-1} (see Figure S1 in supporting information) in Al-BDC MOF is linked to the hydroxyl group bridging the aluminum ions.[35,36]

XRD analysis was carried out for Al-BDC MOF and its nanocomposite with MnO_2, i.e., MnO_2@Al-BDC to investigate their crystallinity and structures. The XRD pattern of the Al-BDC MOF pictured in Figure 2 displays the main diffraction peaks at $2\theta = 9.30°$, 10.58°, 14.87°, 17.26°, 21.24°, 25.10°, and 27.16°. The characteristic reflections of the prepared MOF are matched with those reported before for MIL-53 (Al).[34] However, some peaks are missed while other additional peaks are coexisting. This finding could be due to some differences in the structure and/or the crystallinity as a result of modification of the experimental procedure used for its synthesis. Generally, the characteristic peaks of the synthesized Al-BDC MOF are consistent with those found in the simulated pattern (COD-7000343). On the other hand, the XRD pattern of MnO_2@Al-BDC nanocomposite shows similarly the same reflections. Some shifts in the peak positions together with the appearance of pronounced peaks at other positions may reflect the impact of modification of the MOF with MnO_2. The new peaks are still coinciding with those of the simulated pattern.

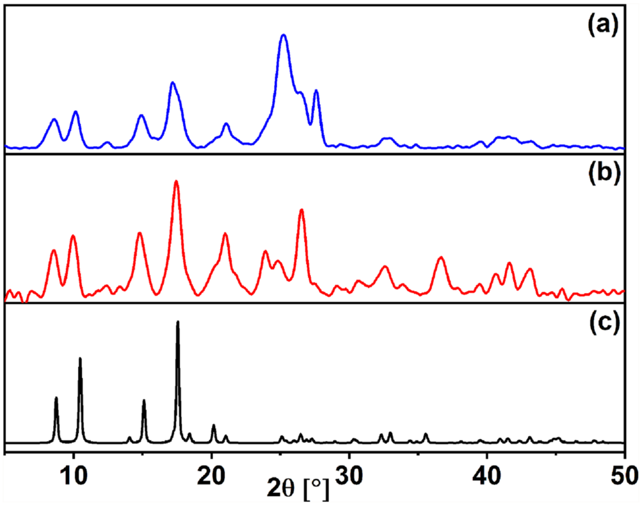

FIGURE 2 XRD patterns of a) Al-BDC MOF, b) MnO_2@Al-BDC nanocomposite, and c) simulated pattern of MIL-53(Al).

The morphology and particle size of MnO_2@Al-BDC nanocomposite were investigated via transmission electron microscopy. The TEM images from different sections of the nanocomposite are displayed in Figure 3. The TEM images show that the nanocomposite has in most cases a sphere-like morphology that is quite obvious in the TEM image positioned on the right. These particles are mainly related to Al-BDC MOF. The particle size of such spheres falls in the range of 20–35 nm signifying the nano-scale formation of Al-BDC MOF. Moreover, the TEM images display also large particles spread over the MOF surface that can be due to the presence of MnO_2 and ascertain its formation on the MOF surface. These particles adopt a sponge-like morphology with a large size of around 100 nm.

The chemical composition of the nanocomposite was investigated via X-ray photoelectron spectroscopy (XPS). The wide-scan XPS spectrum and its magnified and deconvoluted spectra are depicted in Figure 4. The full scanned spectrum manifests the presence of both C and O from the linker, Al from the MOF, and Mn from the MnO_2. This finding demonstrates the formation of MnO_2@Al-BDC nanocomposite. Deconvolution of C 1 s signal results in four Gaussian peaks showing various chemical states of carbon atoms (Figure 4b). A sharp peak found at a binding energy of 284.4 eV is ascribed to C atoms in carbon structure with C–C. Moreover, small peaks apparent at 285.3 eV and 288.7 eV can be related to the carbon from C–O and C=O bond, respectively.[37] Moreover, the peak at 283.2 eV is ascribed to carbon in C=C bond. The deconvoluted XPS spectrum of Al 2p shown in Figure 4c displays two peaks at 74.2 and 75.0 eV related to the octahedral frames of $AlO_4(OH)_2$ clusters in Al-BDC MOF.[38]

Figure 4d illustrates the XPS spectrum of O 1s, it comprises peaks with binding energies located at 529.8, 531.7, and 533.0 eV that can be assigned to Al-O, Mn–O-Mn, and Mn–O-H bonds, respectively.[39] Additionally, the C-O bond may also be identified by the binding energy peak located at 531.7 eV. Finally, Figure 4e exhibits four XPS signals at 655.7, 653.9, 645.3, and 642.5 eV that are related to Mn $2p^{3/2}$ and Mn $2p^{1/2}$ signifying the presence of both Mn^{4+} and Mn^{3+} states.

3.2 | Adsorption properties

3.2.1 | Effect of pH on adsorption process

The adsorption properties of Al-BDC and MnO_2@Al-BDC nanocomposite were examined and tested initially for the removal of iron from water (initial pH was adjusted to 2.2). A 35.0 mg dose was used for this study. The removal efficiency (R %) and adsorption capacity (q_t) were calculated using the subsequent equations:

$$R\% = \frac{(C_o - C_e)}{C_o} \times 100 \tag{1}$$

$$q_t = (C_o - C_e) \times \frac{V}{W} \tag{2}$$

where C_o and C_e (mg/L) are the initial and the equilibrium concentrations of the iron solution, respectively.

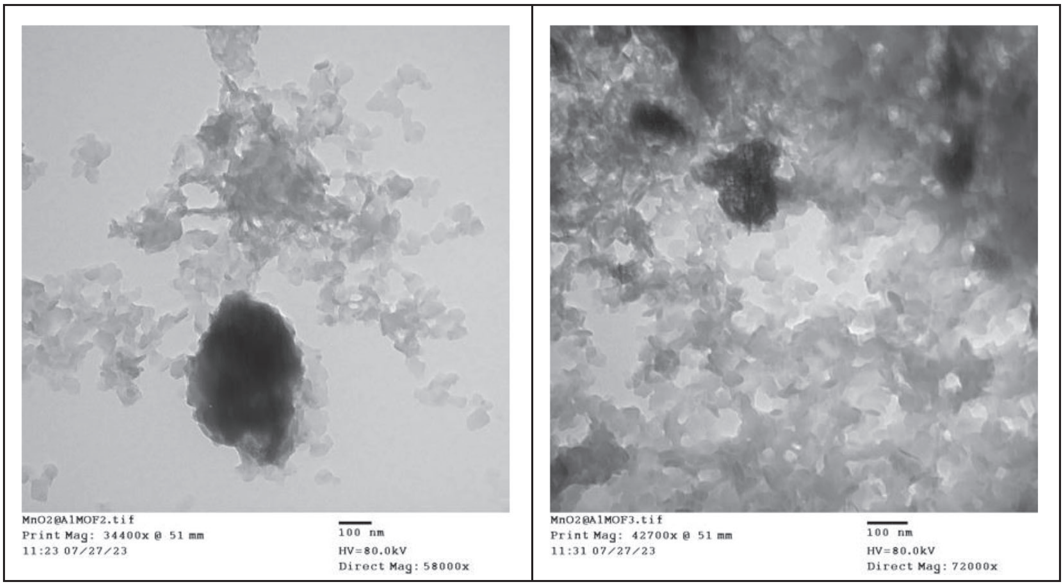

FIGURE 3 TEM images of MnO_2@Al-BDC nanocomposite.

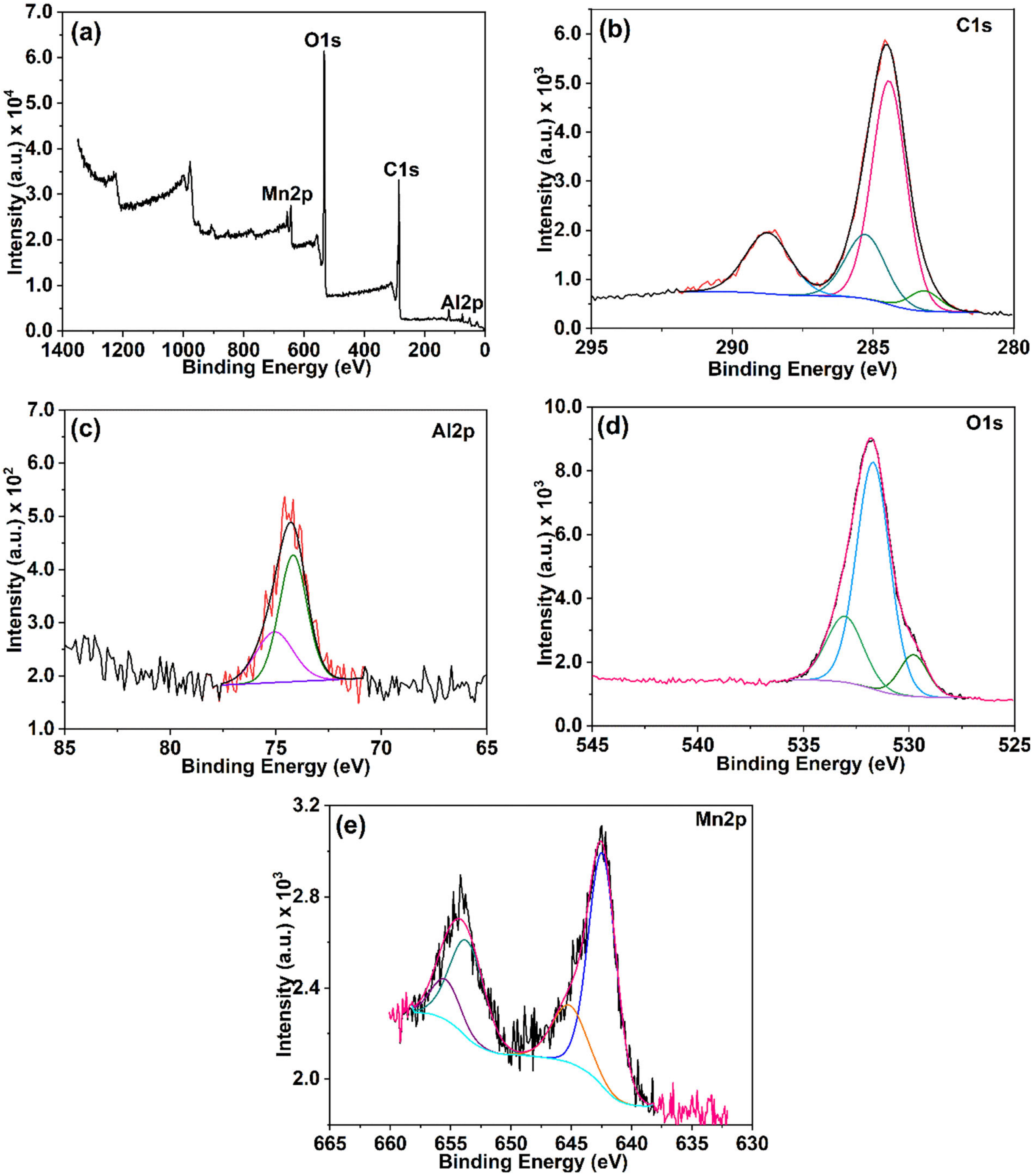

FIGURE 4 XPS analysis of MnO_2@Al-BDC nanocomposite.

W (g) is the weight of the adsorbent, and V (L) is the volume of the solution.

The results showed that Al-BDC MOF (50.0 mg) has a low adsorption capacity for iron and hence the removal of 54.0% of Fe^{3+} (50.0 mL of 5.0 mg/L) ions from the water was attained after 120 min. On the other hand, the removal of Fe^{3+} ions from the water was carried out using MnO_2@Al-BDC nanocomposite employing the following conditions, i.e., initial pH of 2.2, dose of 35.0 mg of the nanocomposite and 50.0 mL of 5.0 mg/L Fe^{3+} solution. The results of Fe^{3+} removal using the nanocomposite are presented in Figure 5a. It is obvious that increasing the contact time results in a noticeable increase in the Fe^{3+} removal percentage. Although, the removal was moderate (~50.0–70.0%) at first 10 min, nevertheless after 120 min it maintained 97.0%. In contrast, at pH of 9.2 removal of 70.0–80.0% of Fe^{3+} was achieved during the first 10 min, and by increasing the contact time to 120 min, it reached only 90.0%. Therefore, all the removal experiments were conducted at pH of 2.2.

The adsorption capacity of nanocomposite was determined at two pH values using the same experimental parameters and the results are pictured in Figure 5b. After 120 min, the q_e value was 6.9 mg. g^{-1} at pH = 2.2, while q_e was 6.5 mg. g^{-1} at pH = 9.2. As shown in Figure 5b, the adsorption capacity of iron obtained at pH = 2.2 is better than that obtained in the alkaline medium. Such higher adsorption capacity in the acidic medium can be ascribed to the presence of MnO_2 particles over the surface that acquire a negative charge originating from surface hydroxyl groups. Iron ions replace the protons covering the surface in this acidic medium to initiate an electrostatic interaction with the negatively charged surface.

3.2.2 | Effect of adsorbent dose

Different doses of 15.0, 35.0, and 50.0 mg from the nanocomposite were applied to study the effect of dose on Fe^{3+} removal from 50 mL solution at pH of 2.2. As demonstrated in Figure 6a, the increase in nanocomposite doses results in an increase in the Fe^{3+} removal %. Definitely, the nanocomposite dose of 50.0 mg demonstrates the highest removal of iron during the first 5 min. Utilizing a dose of 35.0 mg leads to a 50.0% removal of Fe^{3+} in the first 5 min. After 120 min, removal of 97.0% and 98.7% was attained using 35.0 and 50.0 mg doses, respectively. For all doses, the data plotted in Figure 6b reveal that the amount of adsorbed iron increases with contact time. After 120 min, the highest adsorption capacity of 15.0 mg. g^{-1} was achieved using 15.0 mg of the

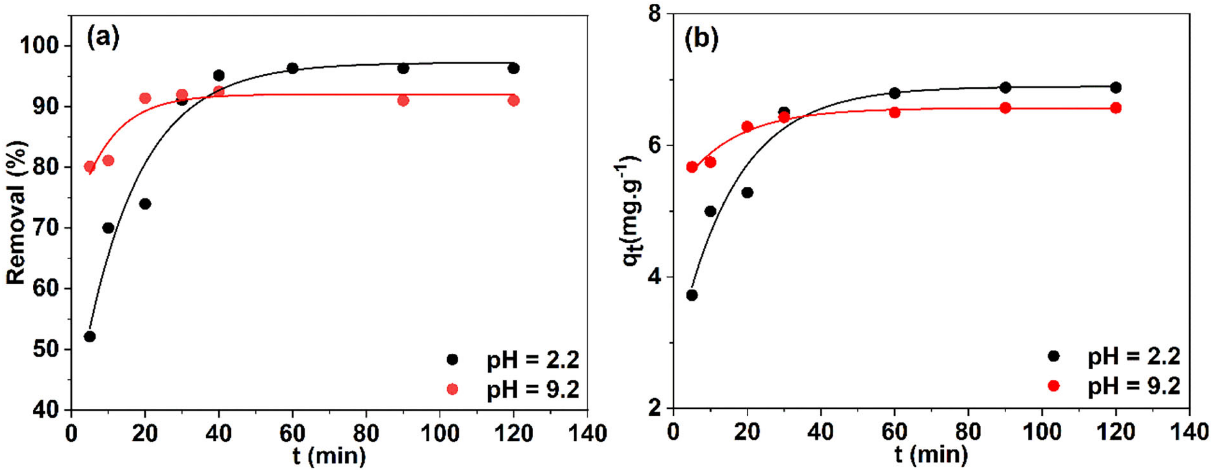

FIGURE 5 (a) Removal% of Fe^{3+} recorded at different contact times at pH = 2.2 and 9.2, 35.0 mg of the nanocomposite and 50.0 mL (5.0 mg/L) of Fe^{3+} solution were used, and (b) Adsorption capacity (mg.g^{-1}) determined at different contact time at pH = 2.2 and 9.2.

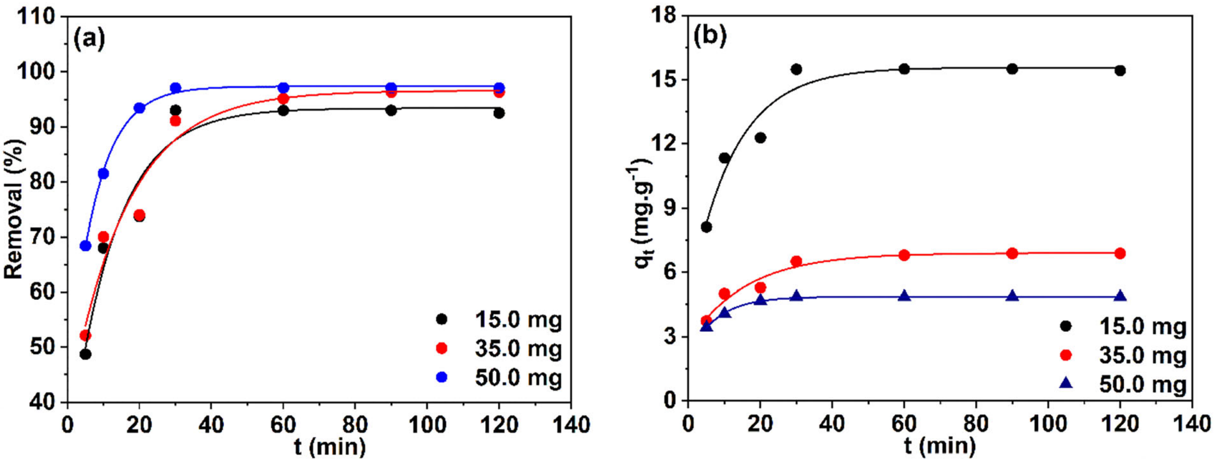

FIGURE 6 (a) Removal% of Fe^{3+} recorded at different contact times using different doses of the nanocomposite, i.e., 15.0, 35.0, and 50.0 mg, and (b) Adsorption capacity (mg.g^{-1}) recorded at different contact times using different nanocomposite doses.

nanocomposite. On the other hand, the amount of adsorbed iron reached 6.0 and 4.0 mg. g^{-1} using 35.0 and 50.0 mg nanocomposite, respectively. The decreased adsorption capacity with increasing the adsorbent dose is in accordance with the fact that the sorption sites tend to be unsaturated and overlapped as the dose of adsorbent increases besides particle aggregation that leads to a reduction in the total surface area of the adsorbent thus reducing adsorbate amount/unit surface area.[40]

3.2.3 | Effect of iron concentration

By applying different iron concentrations, Figure 7a expresses the variation of removal percentage as a function of initial iron concentrations, i.e., 2.7, 5.0, and 7.7 mg/L. In this study, 35.0 mg of the nanocomposite and 50 mL of each concentration of iron aqueous solution were used. During the first 5 min, the highest removal efficiency was attained while using 2.7 mg/L of Fe^{3+} concentration. This may be attributed to the presence of many binding sites on the adsorbent surface. The progress of removal efficiency was slowed down thereafter till 20 min but enhanced after that reaching a value of ~98.0% at 60 min. It deserves to be noted that a removal efficiency of ~98.0% upon utilizing 5.0 mg/L as an initial iron concentration is the same as that attained using 2.7 mg/L iron concentration. No further increase in the efficacy of removal was detected after that even by increasing the contact time to 90 min. On the other side, using an initial concentration of iron as 7.7 mg/L, the removal drops to 85.0% at 90 min.

The results displayed in Figure 7b reveal that the amount of adsorbed iron increases over time for all initial

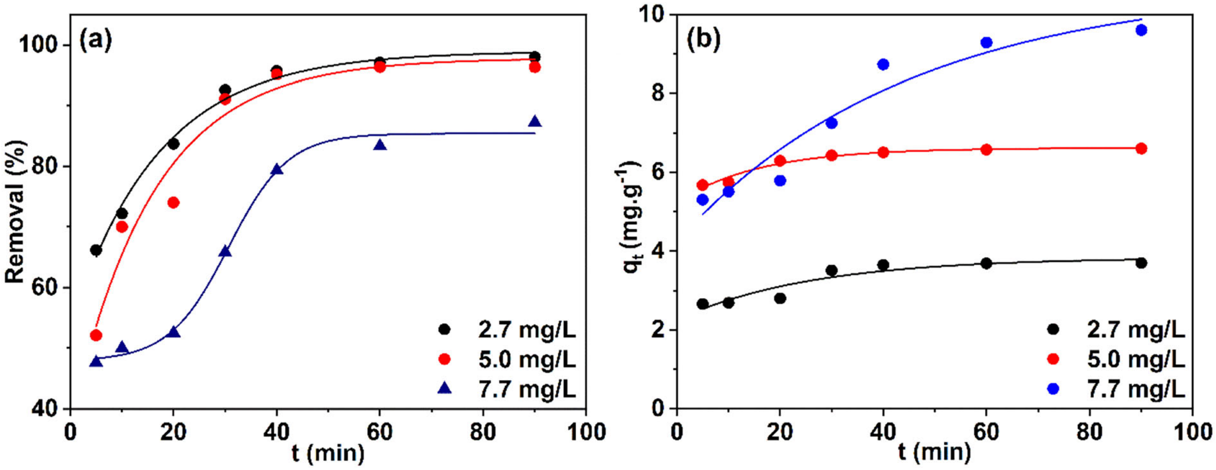

FIGURE 7 (a) Removal% of Fe^{3+} estimated at different contact times using different initial concentrations of iron, i.e., 2.7, 5.0, and 7.7 mg/L, and (b) Adsorption capacity ($mg.g^{-1}$) determined at different contact times using different initial concentrations of iron.

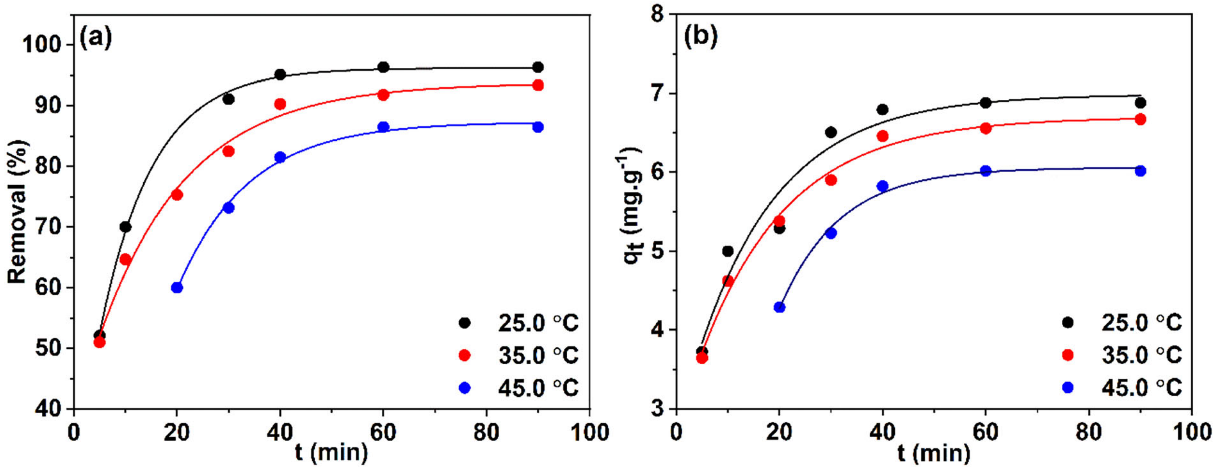

FIGURE 8 (a) Removal% of Fe^{3+} determined at different contact times at different temperatures of 25.0, 35.0, and 45.0 °C, and (b) Adsorption capacity ($mg.g^{-1}$) recorded at different temperatures.

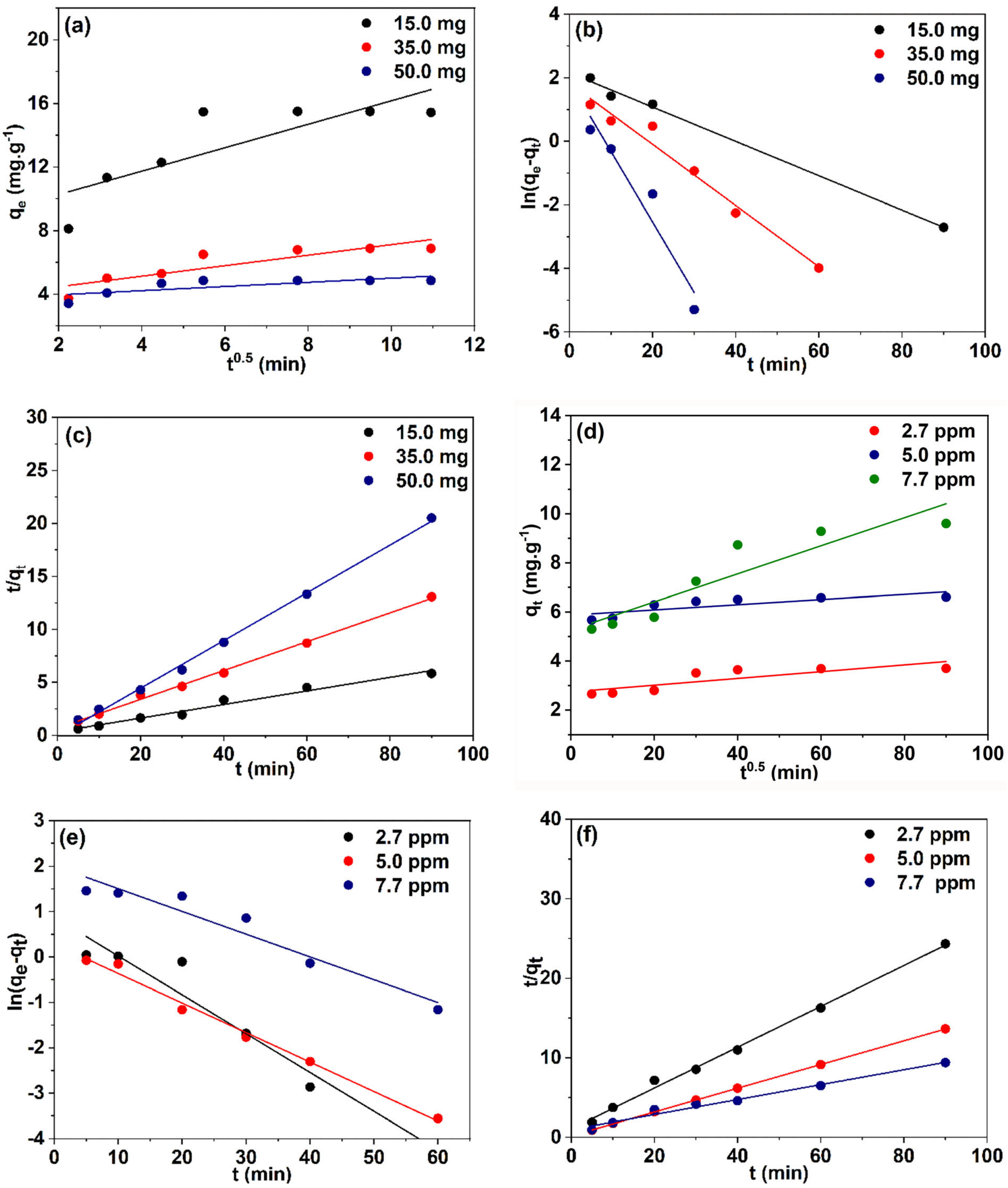

FIGURE 9 (a&d) Intraparticle diffusion mechanism applied to the adsorption data obtained using different doses of MnO_2@Al-BDC nanocomposite, i.e., 15.0, 35.0, 50.0 mg and different iron initial concentrations, i.e., 2.7, 5.0, and 7.7 mg/L, (b&e) applicability of the pseudo-first-order kinetics model to the data obtained using different nanocomposite doses and different iron initial concentrations, and (c&f) applicability of the pseudo-second-order kinetics model to the data obtained using different nanocomposite doses and iron initial concentrations.

iron concentrations. The highest adsorbed quantity of 10.0 mg. g^{-1} was observed while using 7.7 mg/L as the initial iron concentration. The quantity of iron adsorbed on the surface of nanocomposite drops to 6.0 and 3.5 mg. g^{-1} after 90 min in case of initial iron concentration of 5.0 and 2.7 mg/L, respectively. The above findings highlight the fact that MnO_2@Al-BDC nanocomposite is a potentially effective nanoadsorbent for remediating iron from aqueous media contaminated with it at various concentrations.

3.2.4 | Effect of temperature on Fe^{3+} removal

The study was performed at variable temperatures, i.e., 25.0, 35.0, and 45.0 °C. A plot of removal % at different contact times is presented in Figure 8a. This allows observation of the behavior of iron removal as a function of increasing the contact time at each temperature. It is clear from the figure that the removal % is significantly affected by variations in adsorption temperature. The highest removal efficiency was seen at a temperature of 25.0 °C, which is slightly different than at 35.0 °C, whilst the least removal was detected at a temperature of 45.0 °C. This finding signifies the better adsorption properties of the nanocomposite by lowering the temperature which is clear from comparing the three curves in Figure 8a. It is important to note that a higher adsorption capacity is connected with the higher ability of the nanocomposite to remove iron, and this is suggestive of a better system performance. On the other side, the adsorption capacity at each temperature is presented in Figure 8b. This interprets the behavior and variability in adsorption capacity with increasing temperature. As one can see at the temperature 25.0 °C, the nanocomposite shows adsorption capacity better than that obtained using the other two applied temperatures, i.e., 35.0 and 45.0 °C. Comparing the curves, to assess the impact of temperature on the adsorption capacity of the iron, indicates that the removal progress at 25.0 or 35.0 °C is more effective for both removal and adsorption quantity of iron.

3.3 | Adsorption kinetics

The mechanism by which the adsorption of Fe^{3+} on the surface of the MnO_2@Al-BDC nanocomposite proceeds can be described by several models such as mass transfer and chemical reaction. The fitting of the experimental data obtained for the adsorption of iron over the surface of the nanocomposite shows either pseudo-first-order, pseudo-second-order, or the intraparticle diffusion model. The subsequent Weber and Morris equation can be applied to observe the role of the intraparticle diffusion mechanism in the adsorption kinetics.

$$q_t = K_P t^{0.5} + I \tag{3}$$

where q_t is the amount of solute on the surface of the adsorbent at time t (mg. g^{-1}), K_p is the intraparticle rate constant (mg/g $min^{0.5}$), t is the time (min) and I (mg. g^{-1}) is a constant that gives an idea about the thickness of the boundary layer.

A linear relationship between q_t and $t^{0.5}$ should be obtained. The plot of this relation while using different doses (15.0, 35.0, and 50.0 mg) of the nanocomposite as shown in Figure 9a reveals a deviation of data obtained from linearity and even without passing through the origin. The same observation can be seen for this relationship constructed employing different initial iron concentrations as shown in Figure 9d. These findings demonstrate that other mechanisms besides intraparticle diffusion also contribute to the adsorption process.[41]

On the other side, pseudo-first-order kinetics model is generally applied to the aqueous solution with low concentrations. The pseudo-first-order model can be designated by the subsequent equation[42]:

$$\ln(q_e - q_t) = ln q_e - K_1 t \tag{4}$$

where K_1 is the constant speed of adsorption of the pseudo-first-order model (min^{-1}).

TABLE 1 Comparison of adsorption rate constants and estimated and observed q_e values obtained for intraparticle diffusion, pseudo-first-order, and pseudo-second-order models while employing different nanocomposite doses, and different initial iron concentrations.

Kinetics models		Dose (mg)			Initial concentration (ppm)		
		15.0	35.0	50.0	2.7	5.0	7.7
Intraparticle diffusion	**Kp**	0.730	0.330	0.130	0.014	0.010	0.057
	I	8.780	3.800	3.690	2.740	5.874	5.266
	R2	0.690	0.790	0.590	0.695	0.656	0.854
Pseudo-first-order	**q_e (cal)**	8.670	6.230	6.610	2.400	1.330	7.460
	K_1	0.050	0.096	0.220	0.085	0.065	0.050
	R^2	0.990	0.975	0.935	0.950	0.991	0.932
Pseudo-second-order	**q_e (cal)**	15.620	7.350	4.450	3.900	6.700	10.600
	K_2	0.012	0.276	0.310	0.062	0.119	0.009
	R^2	0.979	0.997	0.997	0.996	0.999	0.983

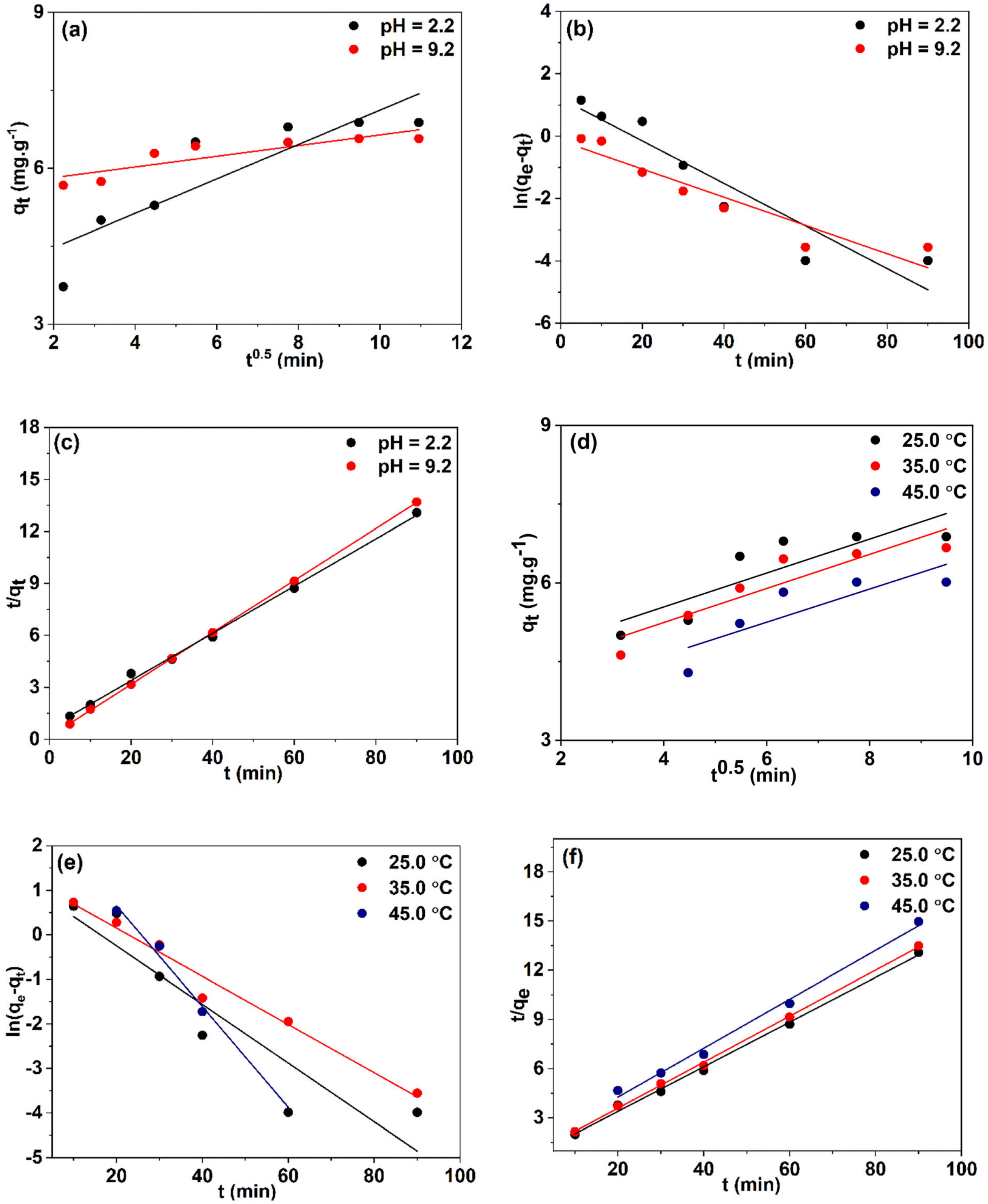

FIGURE 10 (a&d) Intraparticle diffusion mechanism applied to the plots obtained using different initial pH, i.e., 2.2 and 9.2, and reaction temperatures, i.e., 25.0, 35.0, and 45.0 °C (b&e), applicability of the pseudo-first-order kinetics model to the data obtained using different initial pH and reaction temperatures, and (c&f) applicability of the pseudo-second-order kinetics model to the data obtained using different initial pH and reaction temperatures.

When the plot of the relationship between ln (q_e - q_t) and t yields a straight line, the pseudo-first-order kinetics model is applicable in this case. Additionally, the determined intercept should equal ln q_e for an exact pseudo-first-order process. Nonlinear relationships are seen in the plots shown in Figure 9b and 9e. Additionally, the linearly fitted lines' intercepts differ significantly from ln q_e's value. This result implies that the pseudo-first-order

Kinetics models		Temperature			pH	
		25.0	35.0	45.0	2.2	9.2
Intraparticle diffusion	Kp	0.323	0.325	0.316	0.330	0.102
	I	4.246	3.940	3.352	3.810	5.610
	R2	0.740	0.840	0.710	0.780	0.761
Pseudo-first-order	q_e (cal)	2.900	3.430	18.390	3.370	1.190
	K_1	0.066	0.054	0.113	0.068	0.045
	R^2	0.860	0.977	0.971	0.889	0.887
Pseudo-second-order	q_e (cal)	7.350	7.140	6.700	7.350	5.700
	K_1	0.027	0.025	0.017	0.028	0.210
	R^2	0.997	0.999	0.993	0.997	0.999

TABLE 2 A comparison of adsorption rate constants against estimated and observed q_e values obtained for intraparticle diffusion, pseudo-first-order, and pseudo-second-order models while employing different initial pH of the medium, and varied adsorption temperatures.

T (*K*)	ln K_c	Δ*G*° (k J Mol^{-1})	Δ*H*° (k J Mol^{-1})	Δ*S*° (J mol^{-1} K^{-1})	R^2
298.0	0.340	−103.638	−746.424	−2.157	0.975
308.0	0.280	−82.068			
318.0	0.182	−60.498			

TABLE 3 Thermodynamic parameters estimated for the adsorption of Fe^{3+} on the surface of MnO_2@Al-BDC nanocomposite.

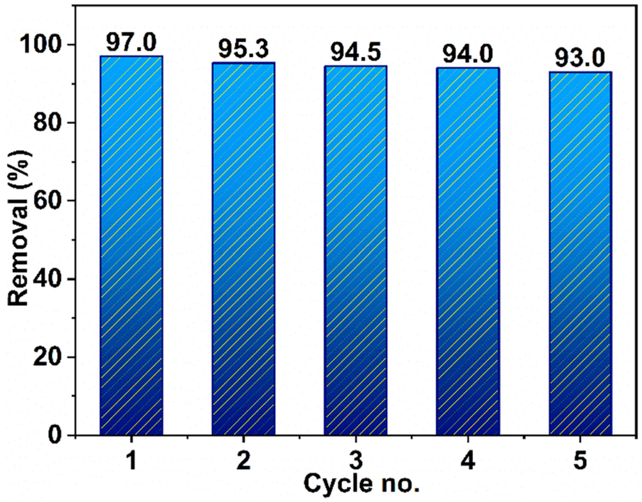

FIGURE 11 Re-usability test of MnO_2@Al-BDC nanocomposite for removal of Fe^{3+} from wastewater.

kinetics is not applicable for the Fe^{3+} adsorption over the surface of different doses of MnO_2@Al-BDC nanocomposite, i.e., 15.0, 35.0, 50.0 mg. The same finding is obvious in the case of adsorption from solutions with different Fe^{3+} initial concentrations, i.e., 2.7, 5.0, and 7.7 mg/L.

The subsequent equation represents the pseudo-second-order model,[43] which is based on the adsorption equilibrium capacity:

$$\frac{t}{q_t} = \frac{1}{K_2 q_e^2} + \frac{t}{q_e} \tag{5}$$

where K_2 is the constant speed of the adsorption model of pseudo-second-order (g mg^{-1} min^{-1}).

A linear relationship with a slope of $1/q_e$ and an intercept of $1/(K_2\ q_e^2)$ should be obtained when plotting t/q_t versus t. Figure 9c and 9f shows typical linear relationships that indicate the applicability of the pseudo-second-order kinetics for the Fe^{3+} adsorption on the surface of different doses of the nanocomposite, i.e., 35.0, 50.0, and 70.0 mg. As well as the pseudo-second-order model is applied while using different iron initial concentrations, i.e., 2.7, 5.0, and 7.7 mg/L.

All parameters obtained by application of the three kinetic models are shown in Table 1 along with the correlation coefficients and the adsorbed quantities. In the case of intraparticle diffusion kinetics model and pseudo-first-order, it is obvious that the quantity adsorbed determined experimentally differs from that calculated. The pseudo-second-order kinetic model demonstrates an agreement between the observed and estimated values of quantity adsorbed. Furthermore, values of R^2 coefficients are very close to unity, which means the adsorption of Fe^{3+} on nanocomposite surface proceeds through pseudo-second-order kinetics.

The applicability of the three models was also studied while carrying out the adsorption process at different initial pH of the medium as well as at varied reaction temperatures, i.e., 25.0, 35.0, and 45.0 °C, the other experimental conditions were kept constant. The plots shown in Figure 10 also show that the pseudo-secondorder model represents the kinetics by which the adsorption process proceeds at different initial pH and similarly at varied reaction temperatures. All parameters obtained by application of the three kinetic models are

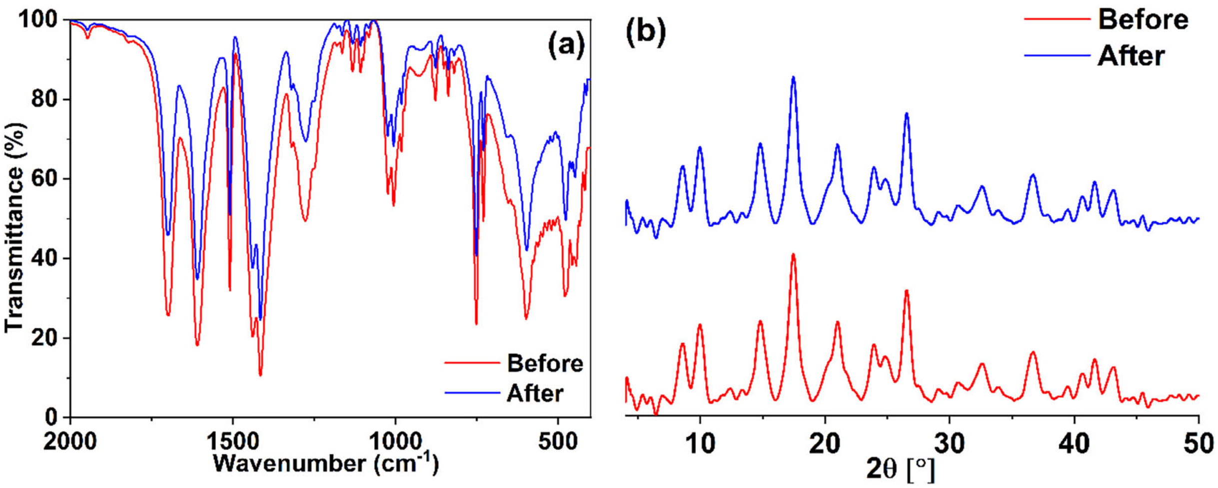

FIGURE 12 IR and XRD analysis of MnO_2@Al-BDC nanocomposite before and after five cycles of Fe^{3+} removal.

shown in Table 2 along with the correlation coefficients and the adsorbed quantities. These results reveal also that the kinetics of the adsorption process follow a pseudo-second-order model.

3.4 | Adsorption thermodynamics

The thermodynamics of Fe^{3+} adsorption on the surface of MnO_2@Al-BDC nanocomposite can be investigated through the variation of the temperature at which the adsorption process takes place. Therefore, the basic thermodynamic parameters, i.e., free energy of the adsorption process (ΔG°), standard entropy (ΔS°), and standard enthalpy (ΔH°) can be determined. Then, the following thermodynamic relationships should be considered.

$$\Delta G^\circ = \Delta H^\circ - T\Delta S^\circ \tag{6}$$

$$K_c = \frac{q_e}{C_e} \tag{7}$$

$$\ln K_c = -\frac{\Delta H^\circ}{RT} + \frac{\Delta S^\circ}{R} \tag{8}$$

where T is the absolute temperature (K) and R is the gas constant (8.314 J mol^{-1} K^{-1}).

A straight line is produced when the relationship between $\ln K_c$ and (1/T) is plotted. The standard enthalpy (ΔH°) can be calculated from the slope of this line. Moreover, the standard entropy (ΔS°) value can be found from its intercept. Table 3 shows the calculated thermodynamic parameters. It is obvious that the ΔG° values determined at various temperatures are negative; indicating the iron adsorption on MnO_2@Al-BDC nanocomposite is a spontaneous process and confirms its feasibility. The more negative is the ΔG° values, the easier is the adsorption process. It can also be seen that ΔH value is negative, revealing that the adsorption of Fe^{3+} on the nanocomposite surface is an exothermic process. Furthermore, during the adsorption process, the ordered arrangement at the solid–liquid interface improves, which is shown by the negative ΔS value.

3.5 | Removal of Fe^{3+} from real water samples

The nanocomposite demonstrated high efficiency in removing Fe^{3+} ions from all provided real water samples. Removal efficiencies of up to 99.0% were achieved, depending on the initial Fe^{3+} ion concentration and sample matrix. The presence of other metal ions and organic matter in the real water samples had a negligible effect on the adsorption performance, indicating the selectivity and robustness of the nanocomposite.

3.6 | Re-usability and stability of MnO_2@Al-BDC nanocomposite

It is of value for any adsorbent material to explore its re-usability, the more it can be reused the more efficient its application. Consequently, we have investigated the possibility of reusing our adsorbent for further adsorption processes. As it can be seen from Figure 11, our adsorbent can be used several times for the removal of Fe^{3+} without appreciable loss of its efficiency for adsorption. A slight decrease in the removal efficacy can be seen after five adsorption cycles.

TABLE 4 Comparison of the adsorption efficiency of MnO_2@Al-BDC nanocomposite with that of some reported adsorbent materials.

	Adsorpent	Dose	Removal conditions	Removal (%)	Ref.
1	Chitosan powder	20.0 mg	50.0 mg/L Fe (III)), 3 h and pH = 2.0	30.0% per 0.02 g of chitosan	[44]
2	Carboxyl-functionalized wood microchannel	20.0 mg	100.0 mg/L Fe (III)), 3 h and pH = 2.5	94.7%	[45]
3	Mn_2O_3/Mn_3O_4 nanocomposite	0.5 g	50.0 mg/L Fe (III), 62.5 min and pH = 5.0	95.8%.	[46]
4	Cubical shaped Zeolite	1.4 g L^{-1}	10.0 mg/L Fe (III), 120 min and pH = 9.0	99.9%	[47]
5	TiO_2 and $TiOF_2$	20.0 mg	1.0 mg/L Fe (III), 90 min and pH = 4.0	99.5%	[48]
6	MnO_2@Al-BDC nanocomposite	35.0 mg	5.0 mg/L Fe (III), 90 min and pH = 2.2	98.7%	**This work**

On the other hand, the nanocomposite showed long-term stability after five cycles of adsorption as proven by both XRD and IR analyses. The IR spectra (Figure 12a) of the nanocomposite before and after five cycles of adsorption showed no difference as well as the XRD patterns shown in Figure 12b for the nanocomposite reveal that it retains its structure after five cycles of adsorption.

Comparison of our MnO_2@Al-BDC nanocomposite as an adsorbent material for the removal of Fe^{3+} from water with those reported in the literature has been made in terms of dosage, duration, and removal effectiveness. The results shown in Table 4 demonstrate that our MnO_2@Al-BDC nanocomposite has a comparable removal efficacy for the elimination of Fe^{3+} from water and can be useful in the elimination of other charged contaminants, i.e., heavy metals.

4 | CONCLUSIONS

In this study, we successfully prepared and characterized a novel MnO_2@Al-BDC nanocomposite. TEM and XPS analyses confirmed the presence of MnO_2 on the surface of the Al-BDC MOF. The Al-BDC MOF was identified by spherical particles of 20–35 nm diameter, while MnO_2 appeared as sponge-like spheres with a diameter of 100 nm. The nanocomposite demonstrated significantly higher activity in removing Fe^{3+} from water compared to the bare Al-BDC MOF. This enhanced performance is attributed to the negatively charged MnO_2 particles, which results from the presence of surface hydroxyl groups. The removal efficiency reached 97.0% within 120 min using 35.0 mg of the nanocomposite and 50.0 mL of 5.0 mg/L Fe^{3+} solution at room temperature. Experimental parameters such as adsorbent dose, Fe^{3+} concentration, and temperature significantly influenced the adsorption capacity, achieving a maximum of 15 mg/g with 15.0 mg of the nanocomposite. Kinetic studies indicated that the adsorption followed a pseudo-second-order mechanism with a correlation coefficient very near to unity. Thermodynamic analysis revealed that the adsorption process was spontaneous and exothermic, with negative values for $\Delta G°$ (−103.638) at 298 K and ΔH (−746.424), while the negative ΔS value (−2.157) suggested an increased order at the solid–solution interface. The nanocomposite exhibited long-term stability and reusability, maintaining 93.0% efficiency after five cycles. Overall, this work introduces a novel and efficient adsorbent material, offering a promising solution for heavy metal remediation and the potential for removing other pollutants from water.

AUTHOR CONTRIBUTIONS

Mohamed I. Said: Conceptualization; investigation; writing—original draft; methodology; validation; visualization; writing—review and editing; software; formal analysis; project administration; data curation; supervision. **Marwa Sayed:** Investigation; writing—original draft; methodology; software; formal analysis; data curation; validation; writing—review and editing; visualization; funding acquisition. **Aref A. M. Aly:** Conceptualization; writing—review and editing; supervision. **Muhammad Atef:** Writing - review and editing; supervision.

DATA AVAILABILITY STATEMENT

Author elects to not share data.

ORCID

Marwa Sayed https://orcid.org/0009-0009-8185-9119
Aref A. M. Aly https://orcid.org/0000-0001-9543-1206
Muhammad Atef https://orcid.org/0009-0002-1576-7477

REFERENCES

[1] S. Mallakpour, E. Azadi, C. M. Hussain, *New J. Chem.* **2021**, *45*, 13247.
[2] D.-W. Lim, M. Sadakiyo, H. Kitagawa, *Chem. Sci.* **2019**, *10*, 16.
[3] E. González-Zamora, I. A. Ibarra, *Mater. Chem. Front.* **2017**, *1*, 1471.
[4] C.-Y. Sun, C. Qin, C.-G. Wang, Z.-M. Su, S. Wang, X.-L. Wang, G.-S. Yang, K.-Z. Shao, Y.-Q. Lan, E.-B. Wang, *Adv. Mater.* **2011**, *23*, 5629.
[5] H. D. Lawson, S. P. Walton, C. Chan, *ACS Appl. Mater. Interfaces* **2021**, *13*, 7004.
[6] Q. Zhu, Y. Chen, W. Wang, H. Zhang, C. Ren, H. Chen, X. Chen, *Sens. Actuators B* **2015**, *210*, 500.
[7] A. H. Rageh, M. Ibrahim, M. I. Said, *Solid State Sci.* **2023**, *140*, 107202.
[8] M.-L. Hu, V. Safarifard, E. Doustkhah, S. Rostamnia, A. Morsali, N. Nouruzi, S. Beheshti, K. Akhbari, *Microporous Mesoporous Mater.* **2018**, *256*, 111.
[9] M. Sánchez-Sánchez, N. Getachew, K. Díaz, M. Díaz-García, Y. Chebude, I. Díaz, *Green Chem.* **2015**, *17*, 1500.
[10] J. E. Efome, D. Rana, T. Matsuura, C. Q. Lan, *Sci. Total Environ.* **2019**, *674*, 355.
[11] J. E. Efome, D. Rana, T. Matsuura, C. Q. Lan, *Chem. Eng. J.* **2018**, *352*, 737.
[12] J. E. Efome, D. Rana, T. Matsuura, C. Q. Lan, *ACS Appl. Mater. Interfaces* **2018**, *10*, 18619.
[13] S. Rojas, P. Horcajada, *Chem. Rev.* **2020**, *120*, 8378.
[14] M. J. Uddin, R. E. Ampiaw, W. Lee, *Chemosphere* **2021**, *284*, 131314.
[15] F. Hooriabad Saboor, N. Nasirpour, S. Shahsavari, H. Kazemian, *Chem. Asian J.* **2022**, *17*, e202101105.
[16] K. M. Alkhamis, M. M. Aljohani, S. F. Ibarhiam, Y. A. S. Hameed, H. M. Abumelha, T. M. Habeebullah, N. M. El-Metwaly, *ACS Omega* **2023**, *8*, 30374.
[17] M. A. Hamouda, S. M. Sheta, R. R. Sheha, A. T. Kandil, O. I. Ali, S. M. El-Sheikh, *RSC Adv.* **2022**, *12*, 13103.
[18] C. Crivello, S. Sevim, O. Graniel, C. Franco, S. Pané, J. Puigmartí-Luis, D. Muñoz-Rojas, *Mater. Horiz.* **2021**, *8*, 168.
[19] F. Yang, M. Du, K. Yin, Z. Qiu, J. Zhao, C. Liu, G. Zhang, Y. Gao, H. Pang, *Small* **2022**, *18*, 2105715.
[20] H. E. H. Ahmed, M. Soylak, *J. Food Compos. Anal.* **2023**, *121*, 105396.
[21] Z. Pinar Gumus, M. Soylak, *TrAC Trends Anal. Chem.* **2021**, *143*, 116417.
[22] H. S. Ibrahim, N. S. Ammar, M. Soylak, M. Ibrahim, *Spectrochim. Acta a Mol. Biomol. Spectrosc.* **2012**, *96*, 413.
[23] S. Nazri, M. Khajeh, A. R. Oveisi, R. Luque, E. Rodríguez-Castellón, M. Ghaffari-Moghaddam, *Sep. Purif. Technol.* **2021**, *259*, 118197.
[24] S. Daliran, M. Ghazagh-Miri, A. R. Oveisi, M. Khajeh, S. Navalón, M. Âlvaro, M. Ghaffari-Moghaddam, H. Samareh Delarami, H. García, *ACS Appl. Mater. Interfaces* **2020**, *12*, 25221.
[25] A. Amini, M. Khajeh, A. R. Oveisi, S. Daliran, M. Ghaffari-Moghaddam, H. S. Delarami, *J. Ind. Eng. Chem.* **2021**, *93*, 322.
[26] M. Nozohour Yazdi, S. Dadfarnia, A. M. Haji Shabani, *J. Environ. Chem. Eng.* **2021**, *9*, 104696.
[27] P. A. Kobielska, A. J. Howarth, O. K. Farha, S. Nayak, *Coord. Chem. Rev.* **2018**, *358*, 92.
[28] E. Moumen, L. Bazzi, S. El Hankari, *Proc. Safety Environ. Prot.* **2022**, *160*, 502.
[29] C. Zhang, Y. Yan, Q. Pan, L. Sun, H. He, Y. Liu, Z. Liang, J. Li, *Dalton Trans.* **2015**, *44*, 13340.
[30] X. Zhao, X. Yu, X. Wang, S. Lai, Y. Sun, D. Yang, *J. Chem. Eng.* **2021**, *407*, 127221.
[31] C. Petit, T. J. Bandosz, *J. Mater. Chem.* **2009**, *19*, 6521.
[32] Guidelines for Drinking-Water Quality, *Fourth Edition Incorporating the First Addendum*, World Health Organization, Geneva **2017**.
[33] W. C. Lipps, E. B. Braun-Howland, T. E. Baxter. Standard methods for the examination of water and wastewater, 24th edition, (**2022**).
[34] T. Loiseau, C. Serre, C. Huguenard, G. Fink, F. Taulelle, M. Henry, T. Bataille, G. Férey, *Chem. A Eur. J.* **2004**, *10*, 1373.
[35] T. Lu, H. Song, X. Dong, J. Hu, Y. Lv, *J. Mater. Chem. C* **2017**, *5*, 9465.
[36] C. Li, Z. Xiong, J. Zhang, C. Wu, *J. Chem. Eng. Data* **2015**, *60*, 3414.
[37] M. Liu, Q. Zhao, H. Liu, J. Yang, X. Chen, L. Yang, Y. Cui, W. Huang, W. Zhao, A. Song, Y. Wang, S. Ding, Y. Song, G. Qian, H. Chen, F. Pan, *Nano Energy* **2019**, *64*, 103942.
[38] A. Khodayari, S. Sohrabnezhad, *J. Solid State Chem.* **2021**, *297*, 122087.
[39] Y. Liu, X. Chi, Q. Han, Y. Du, J. Huang, Y. Liu, J. Yang, *J. Power Sources* **2019**, *443*, 227244.
[40] S. Çınar, Ü. H. Kaynar, T. Aydemir, S. Çam Kaynar, M. Ayvacıklı, *Int. J. Biol. Macromol.* **2017**, *96*, 459.
[41] J. Weber Walter, J. C. Morris, *J. Sanit. Eng. Div.* **1963**, *89*, 31.
[42] R.-L. Tseng, P.-H. Wu, F.-C. Wu, R.-S. Juang, *Chem. Eng. J.* **2014**, *237*, 153.
[43] T. Shahwan, *J. Environ. Chem. Eng.* **2014**, *2*, 1001.
[44] A. Burke, E. Yilmaz, N. Hasirci, O. Yilmaz, *J. Appl. Polym. Sci.* **2002**, *84*, 1185.
[45] H. Yuan, L. Xing, J. Wei, Z. Zhao, J. Wang, H. Gao, Y. Nie, *J. Environ. Chem. Eng.* **2023**, *11*, 110348.
[46] N. Samadani Langeroodi, Z. Farhadravesh, A. Dehno Khalaji, *Green Chem. Lett. Rev.* **2018**, *11*, 404.
[47] N. S. Samanta, S. Banerjee, P. Mondal, U. Anweshan, M. K. P. Bora, *Adv. Powder Technol.* **2021**, *32*, 3372.
[48] H. Gomaa, M. A. Shenashen, H. Yamaguchi, A. S. Alamoudi, M. Abdelmottaleb, M. F. Cheira, T. A. Seaf El-Naser, S. A. El-Safty, *J. Clean. Prod.* **2018**, *182*, 910.

SUPPORTING INFORMATION

Additional supporting information can be found online in the Supporting Information section at the end of this article.

How to cite this article: M. I. Said, M. Sayed, A. A. M. Aly, M. Atef, *Appl Organomet Chem* **2024**, e7639. https://doi.org/10.1002/aoc.7639